J. Fluid Mech. (1974), *vol.* 65, *part* 4, *pp.* 711–734
Printed in Great Britain

Laminar flow past an abruptly accelerated elliptic cylinder at 45° incidence

By H. J. LUGT AND H. J. HAUSSLING

Naval Ship Research and Development Center, Washington D.C. 20034

(Received 22 June 1973 and in revised form 28 March 1974)

Numerical solutions for laminar incompressible fluid flows past an abruptly started elliptic cylinder at 45° incidence are presented. Various finite-difference schemes for the stream-function/vorticity formulation are used and their merits briefly discussed. Almost steady-state solutions are obtained for $Re = 15$ and 30, whereas for $Re = 200$ a Kármán vortex street develops. The transient period from the start to the steady or quasi-steady state is investigated in terms of patterns of streamlines and lines of constant vorticity and drag, lift and moment coefficients.

1. Introduction

Time-dependent laminar flows of an incompressible fluid past elliptic cylinders of infinite span at 45° incidence have been analysed by numerical methods. An outline of the procedure used and some initial results were published in a recent note (Lugt & Haussling 1971). In this paper experience gained in the application of the numerical techniques is summarized and the computed results are presented and discussed. The numerical solutions are supported by some experimental data obtained by Honji (1972).

The literature on vortex shedding behind bodies is extensive. The survey papers by Morkovin (1964), v. Krzywoblocki (1966) and Berger & Wille (1972) should be mentioned. However, the onset and the process of vortex shedding behind bodies which are positioned asymmetrically relative to the main flow are not well understood. In particular, details on how the Kutta condition for viscous flows past airfoil-type bodies is established and how the initial vortex is generated and shed are missing from the literature. Furthermore, the period of transition of flows past abruptly started bodies towards a steady state (if it exists) can be monotonic as well as oscillatory depending on the value of the Reynolds number. For symmetric motions the transient phase of flows past abruptly started bodies is always monotonic. Since numerical computations of the kind discussed in this paper are costly the special case of 45° incidence was selected. It seems representative for asymmetric flows. A recent investigation by Mehta & Lavan (1972) which appeared during the writing of this paper supplements the findings of the authors with results for a Reynolds number of 1000 and an angle of attack of 15°.

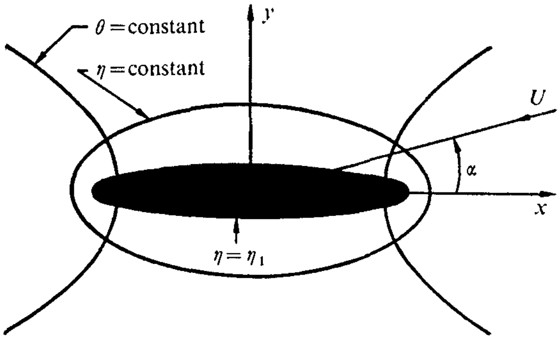

FIGURE 1. Elliptic co-ordinate system and definition of angle of attack α.

2. The flow problem

The developing flow due to abruptly starting an elliptic cylinder of infinite span in an unbounded incompressible fluid is considered. Mathematically, an initial/boundary-value problem for the two-dimensional Navier–Stokes equations must be solved. This solution is conveniently carried out in the elliptic co-ordinate system (η, θ) (figure 1), which is defined by the transformation

$$x + iy = a\cosh(\eta + i\theta), \quad a > 0, \tag{1}$$

where a is the focal distance. The equations of motion are formulated in terms of the dimensionless stream function ψ and ω, the dimensionless vorticity component normal to the η, θ plane:

$$\frac{\partial\omega}{\partial t} + \frac{1}{h^2}\frac{\partial(\psi, \omega)}{\partial(\eta, \theta)} = \frac{2}{Re}\nabla^2\omega, \tag{2}$$

$$\nabla^2\psi = \omega. \tag{3}$$

Here, t is the dimensionless time and $Re = 2aU/\nu$ is the Reynolds number where ν is the kinematic viscosity and U the magnitude of the constant velocity at infinity. (Sometimes, the Reynolds number $Re_d \equiv dU/\nu$ with $d = 2a\cosh\eta_1$ is used for practical reasons. In most cases considered in this paper $\eta_1 = 0{\cdot}1$, so that $Re \approx Re_d$.) The characteristic length and velocity scales in the dimensionless quantities are a and U, respectively. In particular, ∇ is made dimensionless using the length a. The coefficient h is defined by $h^2 = \cosh^2\eta - \cos^2\theta$.

The contour of the ellipse is the constant co-ordinate line $\eta = \eta_1$ (figure 1). An infinitely thin plate is represented by $\eta_1 = 0$ while for a circular cylinder $\eta_1 = \infty$. On this line boundary conditions are prescribed such that the velocity vector $\mathbf{v}$ is zero. The dimensionless velocity components v_η and v_θ are related to ψ by the equations

$$v_\eta = -h^{-1}\partial\psi/\partial\theta, \quad v_\theta = h^{-1}\partial\psi/\partial\eta. \tag{4}$$

Thus, at the body surface the boundary conditions are

$$\psi = \partial\psi/\partial\eta = 0 \quad \text{at} \quad \eta = \eta_1. \tag{5}$$

Here, the constant value of ψ is chosen to be zero. Far away from the body, a uniform parallel flow with velocity $\mathbf{U}$ is assumed, where the vector $\mathbf{U}$ is specified by α and U (figure 1). In terms of ψ the conditions are

$$\partial\psi/\partial\eta = h\sin(\theta-\alpha), \quad \partial\psi/\partial\theta = h\cos(\theta-\alpha) \quad \text{at} \quad \eta = \infty. \tag{6}$$

The initial condition shall simulate the state after the abrupt start of the body in the infinitesimal time span from $t = 0-$ (when the fluid is at rest) to $t = 0+$ (when the irrotational disturbance is felt in the entire field owing to the infinite speed of sound). Thus, at $t = 0+$ the initial condition consists of the potential-flow solution and a vorticity sheet at the body surface which is due to the adherence of the fluid to the surface.

In order to compute the drag, lift and torque on the body by means of flow quantities at the body surface, the pressure distribution on the surface of the body must be determined. From the Navier–Stokes equations it follows that

$$\nabla p = -\frac{2}{Re}\nabla\times\boldsymbol{\omega} - \frac{\partial \mathbf{v}}{\partial t} - \nabla\left(\frac{\mathbf{v}^2}{2}\right) + \mathbf{v}\times\boldsymbol{\omega}, \tag{7}$$

where $\boldsymbol{\omega}$ is the dimensionless vorticity vector and the pressure has been made dimensionless using ρU^2. The quantity ρ is the density of the fluid. The surface pressure is computed from the θ component of (7) to be

$$p_1 = p_c + \frac{2}{Re}\int_{\frac{1}{2}\pi}^{\theta}\left(\frac{\partial\omega}{\partial\eta}\right)_1 d\overline{\theta}, \tag{8}$$

where p_c is the pressure at $(\eta_1, \frac{1}{2}\pi)$, a subscript 1 denotes a value at η_1 and the integral represents the dimensionless vorticity flux over the surface interval from $\frac{1}{2}\pi$ to θ. The point $(\eta_1, \frac{1}{2}\pi)$ is selected for numerical reasons. The pressure p_c is obtained from the η component of (7) by prescribing the value of p at $\eta = \infty$ to be $p_\infty = 0$:

$$p_c = \int_{\eta_1}^{\infty}\left[\frac{2}{Re}\frac{\partial\omega}{\partial\theta} + h\frac{\partial v_\eta}{\partial t} - hv_\theta\,\omega\right]d\eta + \tfrac{1}{2}. \tag{9}$$

The drag coefficient is defined by

$$C_D = \text{drag}/\tfrac{1}{2}\rho U^2 a\cosh\eta_1 \tag{10}$$

and consists of two parts, the drag coefficient due to pressure and that due to friction: $C_D = C_{DP} + C_{DF}$, with

$$C_{DP} = -2\tanh\eta_1\cos\alpha\int_0^{2\pi} p_1\cos\theta\,d\theta - 2\sin\alpha\int_0^{2\pi} p_1\sin\theta\,d\theta, \tag{11}$$

$$C_{DF} = \frac{4}{Re}\left[-\cos\alpha\int_0^{2\pi}\omega_1\sin\theta\,d\theta + \tanh\eta_1\sin\alpha\int_0^{2\pi}\omega_1\cos\theta\,d\theta\right]. \tag{12}$$

Equation (11) is simplified by means of (8) to become

$$C_{DP} = \frac{4}{Re}\left[\tanh\eta_1\cos\alpha\int_0^{2\pi}\left(\frac{\partial\omega}{\partial\eta}\right)_1\sin\theta\,d\theta - \sin\alpha\int_0^{2\pi}\left(\frac{\partial\omega}{\partial\eta}\right)_1\cos\theta\,d\theta\right]. \tag{13}$$

Correspondingly, the lift coefficient is

$$C_L = \text{lift}/\tfrac{1}{2}\rho U^2 a\cosh\eta_1, \tag{14}$$

with

$$C_{LP} = \frac{4}{Re}\left[-\tanh\eta_1\sin\alpha\int_0^{2\pi}\left(\frac{\partial\omega}{\partial\eta}\right)_1\sin\theta\,d\theta - \cos\alpha\int_0^{2\pi}\left(\frac{\partial\omega}{\partial\eta}\right)_1\cos\theta\,d\theta\right], \tag{15}$$

$$C_{LF} = \frac{4}{Re}\left[\sin\alpha\int_0^{2\pi}\omega_1\sin\theta\,d\theta + \tanh\eta_1\cos\alpha\int_0^{2\pi}\omega_1\cos\theta\,d\theta\right]. \tag{16}$$

The moment coefficient is

$$C_M = \mathrm{torque}/\tfrac{1}{2}\rho U^2 a^2 \cosh^2 \eta_1, \tag{17}$$

with

$$C_{MP} = \frac{2}{Re\cosh^2\eta_1}\int_0^{2\pi}\left(\frac{\partial\omega}{\partial\eta}\right)_1 \sin^2\theta\, d\theta, \tag{18}$$

$$C_{MF} = \frac{4}{Re}\tanh\eta_1\int_0^{2\pi}\omega_1\, d\theta. \tag{19}$$

3. Numerical analysis

The infinite domain of integration in the η, θ plane is replaced by a finite network of points specified by $(\eta_1+(i-1)\Delta\eta, (j-\frac{1}{2})\Delta\theta)$, with $i = 1, \ldots, L$ and $j = 1, \ldots, M$. The differential equations are replaced by difference equations involving the values of the variables at these grid points. For all cases $L = 75$ and $\Delta\eta = 0{\cdot}05$, but various values of $M (\equiv 2\pi/\Delta\theta)$ are used. For small η_1 the outer boundary $\eta = \eta_L = \eta_1 + (L-1)\Delta\eta$ is about 11 plate lengths from the body centre. There are no grid points specified at the tips of the ellipse. Earlier numerical computations for ellipses with high curvature ($\eta_1 < 0{\cdot}1$) revealed a much greater numerical stability for a grid which excluded the tip points than for a grid which included these points on the boundary (Lugt & Ohring 1971). In this reference, curves for the surface vorticity and surface pressure are presented for grids with and without tip points. The agreement is very good. Computations for $\eta_1 = 0$ are possible only when there are no grid points at the tips.

The numerical solution of the initial/boundary-value problem stated in the previous section poses two essential difficulties: the approximation of the differential operators in (2) and (3) through suitable difference schemes, and the prescription of boundary conditions for the outer boundary, where $\eta = \eta_L < \infty$ in the numerical scheme. There is no general numerical technique to resolve these problems. For the vorticity equation (2) two popular methods have been examined: the implicit Peaceman–Rachford scheme and the explicit Du Fort–Frankel scheme (Roache 1972, pp. 61 and 91). With the first technique the time increment Δt is limited by the number of iterations needed for obtaining accurate values $\omega_{1,j}$; with the second one the solution becomes unstable beyond a certain value $\Delta t_{\max}$ of Δt. It is found that the DuFort–Frankel scheme for the problem studied is 20–40 % more efficient than the Peaceman–Rachford method while the accuracy is the same. Therefore, the DuFort–Frankel scheme is applied. Equation (2) yields, when solved for $\omega_{i,j}$ at the $(n+1)$th time step, the system of equations

$$\begin{aligned}\omega_{i,j}^{n+1} = {} & \left[\frac{1}{2\Delta t}+\frac{2}{Re\,h_{i,j}^2}\left(\frac{1}{(\Delta\eta)^2}+\frac{1}{(\Delta\theta)^2}\right)\right]^{-1} \\ & \times\left[\frac{\omega_{i,j}^{n-1}}{2\Delta t}+\frac{2}{Re\,h_{i,j}^2}\left\{\frac{1}{(\Delta\eta)^2}(\omega_{i+1,j}^n-\omega_{i,j}^{n-1}+\omega_{i-1,j}^n)\right.\right. \\ & \left.\left. +(\Delta\theta)^{-2}(\omega_{i,j+1}^n-\omega_{i,j}^{n-1}+\omega_{i,j-1}^n)\right\}-J_{i,j}\right],\end{aligned} \tag{20}$$

where the the Jacobian is

$$J_{i,j} = \frac{1}{h_{i,j}^2}\left[\frac{1}{2\Delta\eta}\{(hv_\eta\omega)_{i+1,j}-(hv_\eta\omega)_{i-1,j}\}+\frac{1}{2\Delta\theta}\{(hv_\theta\omega)_{i,j+1}-(hv_\theta\omega)_{i,j-1}\}\right] \tag{21}$$

and the velocity components are

$$(v_\eta)_{i,j} = -\frac{1}{h_{i,j}}\frac{\psi_{i,j+1}-\psi_{i,j-1}}{2\Delta\theta}, \quad (v_\theta)_{i,j} = \frac{1}{h_{i,j}}\frac{\psi_{i+1,j}-\psi_{i-1,j}}{2\Delta\eta}. \tag{22}$$

It is recognized that central-difference schemes for the Jacobian cause oscillations in ω which result in 'cancer cells' (Rimon 1969). These oscillations destroy the quality of the solutions for larger Reynolds numbers unless smaller space increments are employed. Hence, the capacity of the computer sets an upper limit on the Reynolds number. With the space increments $\Delta\eta = 0{\cdot}05$ and $\Delta\theta \simeq 6°$ generally used in this report, the upper limit is about $Re_d = 500$. Mehta & Lavan's (1972) grid is denser near the body in order to resolve the higher vorticity gradients which occur at $Re_d = 1000$. However, their grid is much coarser than the present grid in the region away from the body. Thus, Mehta & Lavan could simulate with accuracy only the early phase of the flow at $Re_d = 1000$ when vorticity is confined to the vicinity of the body.

Equation (3) is approximated by a five-point formula which yields for $\psi_{i,j}$

$$\psi_{i,j} = \tfrac{1}{2}((\Delta\eta)^2+(\Delta\theta)^2)^{-1}[(\Delta\theta)^2(\psi_{i+1,j}+\psi_{i-1,j}) + (\Delta\eta)^2(\psi_{i,j+1}+\psi_{i,j-1}) - (\Delta\eta\Delta\theta)^2h^2_{i,j}\omega_{i,j}]. \tag{23}$$

The system of algebraic equations (23) is solved in three ways. The first method is the Gauss–Seidel successive line overrelaxation (SLOR) applied along lines of constant η. See for instance Roache (1972, p. 119). The overrelaxation factor is 1·82. The iteration process is halted after the kth iteration if

$$|\nabla^2\psi^k - \omega^k| < \epsilon \tag{24}$$

at each grid point, where ϵ is of the order 10^{-3} or 10^{-4}. The number of iterations depends on the nature of the flow field. For $Re = 200$, $\alpha = 45°$, $\eta_1 = 0{\cdot}1$ and $\epsilon = 0{\cdot}002$ the growth of the vortices attached behind the body requires about 60 iterations per time step, whereas vortex separation needs about 130 iterations.

During the course of this study it was found (Lugt & Ohring 1973) that use of either the Buneman algorithm (Buzbee, Golub & Nielson 1970) or the Fourier analysis/cyclic reduction technique (Hockney 1970) is superior to SLOR in terms of efficient use of computer time. Buneman's solution process corresponds on a CDC 6700 computer to 8 iterations with SLOR for the 75 × 64 grid. With 60–130 iterations per time step for SLOR the Buneman method is about 7·5–16 times faster. Hockney's technique is even twice as fast as Buneman's! In addition, SLOR is not as accurate as the other two methods if $\epsilon = 0{\cdot}002$.

For most cases in which SLOR is applied M is taken to be 60 and thus $\Delta\theta = \frac{1}{30}\pi$. In special instances $M = 80$ is chosen. The Buneman and Hockney methods require, respectively, the following numbers of grid points in each co-ordinate direction: L arbitrary with $M = 2^m$ (or vice versa, where m is an integer); $(L-1) = M = 3\times 2^m$ or 2^m. In the present study $L = 75$ with $M = 64$ for Buneman's method; $(L-1) = M = 96$ for Hockney's method, which is used only as a test case.

At the body surface a one-sided difference scheme must be used in order to calculate the vorticity $\omega_{1,j}$. That this approximation strongly affects the numerical stability of the DuFort–Frankel scheme was demonstrated in a previous investigation (Lugt & Rimon 1970). By trial and error it was found that the formula

$$\omega_{1,j} = [4h_{1,j}^2(\Delta\eta)^2]^{-1}(\psi_{2,j}+4\psi_{3,j}-\psi_{4,j}) \tag{25}$$

yields the best results. This equation is derived from the Taylor series expansions with the no-slip condition $(\partial\psi/\partial\eta)_{1,j} = 0$ incorporated:

$$\left.\begin{aligned}\left(\frac{\partial\psi}{\partial\eta}\right)_{2,j} &= \left(\frac{\partial^2\psi}{\partial\eta^2}\right)_{1,j}\Delta\eta+\frac{1}{2}\left(\frac{\partial^3\psi}{\partial\eta^3}\right)_{1,j}(\Delta\eta)^2+O[(\Delta\eta)^3],\\ \left(\frac{\partial\psi}{\partial\eta}\right)_{3,j} &= 2\left(\frac{\partial^2\psi}{\partial\eta^2}\right)_{1,j}\Delta\eta+2\left(\frac{\partial^3\psi}{\partial\eta^3}\right)_{1,j}(\Delta\eta)^2+O[(\Delta\eta)^3].\end{aligned}\right\} \tag{26}$$

By using $\omega_{1,j} = (h^{-2}\,\partial^2\psi/\partial\eta^2)_{1,j}$ and replacing $(\partial\psi/\partial\eta)_{i,j}$ with

$$(2\Delta\eta)^{-1}(\psi_{i+1,j}-\psi_{i-1,j})+O[(\Delta\eta)^2] \tag{27}$$

one arrives at (25). Hence, Taylor series expansions are used which result in an expression for $\omega_{1,j}$ with error of second order in $\Delta\eta$. However, when first derivatives at inner points are replaced by finite differences, the final formula for $\omega_{1,j}$ is of the first order. The hybrid form (25) is more stable than the first-order approximation

$$\omega_{1,j} = 2\psi_{2,j}/h_{1,j}^2(\Delta\eta)^2+O(\Delta\eta) \tag{28}$$

used by most other investigators and much more stable than second-order approximations investigated, for instance,

$$\omega_{1,j} = [2h_{1,j}^2(\Delta\eta)^2]^{-1}(8\psi_{2,j}-\psi_{3,j})+O(\Delta\eta)^2]. \tag{29}$$

In fact, it was found that Δt_{max} is about 10 times smaller for (28) and 100 times smaller for (29) than Δt_{max} for (25). However, the statement that (25) is superior to (28) when used with the DuFort–Frankel scheme is not valid in general. For instance, in other work (Lugt & Haussling 1972) it was found that (25) and (28) were comparable with regard to stability. In this instance, plane wall boundaries occur. It is thus conjectured that the curvature of the surface is important when comparing the usefulness of (25) and (28).

Since the domain of numerical integration is bounded, severe difficulties are encountered in prescribing the conditions at the outer boundary $\eta = \eta_L$. This boundary is almost circular and is divided in half. On the upstream half of the boundary, conditions (6) are used with the alteration that the second condition is replaced by vanishing vorticity:

$$\partial\psi/\partial\eta = h\sin(\theta-\alpha), \quad \omega = 0 \quad \text{on} \quad \eta = \eta_L, \quad \begin{cases} 0 \leqslant \theta \leqslant \frac{1}{2}\pi+\alpha, \\ \frac{3}{2}\pi+\alpha \leqslant \theta < 2\pi. \end{cases} \tag{30}$$

In difference form

$$(\partial\psi/\partial\eta)_{L,j} = h_{L,j}\sin[(j-\tfrac{1}{2})\Delta\theta-\alpha], \quad \omega_{L,j} = 0. \tag{31}$$

On the downstream half of the boundary $\partial\psi/\partial\eta$ and ω cannot be prescribed as in (30). Some time after the abrupt start, depending on the size of the computational region, vorticity and associated deviations from parallel flow reach the downstream boundary. The boundary conditions must allow $\partial\psi/\partial\eta$ and ω to vary with time. The inclusion of this time variation is achieved by using conditions which represent the convection of vorticity and momentum across the border with velocity **U**. Such a condition was proposed by Dawson & Marcus (1970) for the vorticity only and is applied here as follows:

$$\frac{\partial\omega}{\partial t}+\frac{1}{U}(\mathbf{U}.\nabla)\,\omega = 0 \quad \text{on} \quad \eta = \eta_L, \quad \tfrac{1}{2}\pi+\alpha < \theta < \tfrac{3}{2}\pi+\alpha. \tag{32}$$

For ψ they prescribed parallel streamlines. In this paper the idea of convecting flow quantities across the border is extended to the θ component of momentum to give a time-dependent boundary condition for $\partial\psi/\partial\eta$:

$$\left[\frac{\partial\mathbf{v}}{\partial t}+\frac{1}{U}(\mathbf{U}.\nabla)\,\mathbf{v}\right]_\theta = 0. \tag{33}$$

The conditions (32) and (33) replace the conditions of (6). Both (32) and (33) follow from the argument that near the outer boundary diffusion is small, and the flow is approximately steady in a reference frame moving with the free-stream velocity **U**. Then, the momentum equation is

$$(\mathbf{v}-\mathbf{U}/U).\nabla\mathbf{v}+\nabla p = 0. \tag{34}$$

Subtracting (34) from (7) with no diffusion and taking the θ component of the result yields (33). Condition (32) is justified similarly by using the vorticity equation. It is believed that the boundary conditions (32) and (33) come closer to the actual boundary conditions (which are unknown for a finite domain until the complete problem is solved!) than previously used conditions which have been reported in the literature. For example, methods which prescribe vanishing vorticity and even those which require only parallel flow impose unrealistic restrictions for vorticity shedding which are not present in (32) and (33). Mehta & Lavan (1972) modified the boundary conditions (32) and (33), which were published in Lugt & Haussling (1971), by replacing the free-stream velocity $\mathbf{U}/U$ with the local velocity $\mathbf{v}$. The use of the local velocity $\mathbf{v}$ implies that ∇p is neglected. However, experiments by Timme (1957) revealed that the vortices which are shed downstream are of Hamel–Oseen type and thus have a pressure distribution with non-vanishing ∇p. The Hamel–Oseen type of behaviour is also indicated by the numerical results in this paper and is discussed below (figure 16). A further argument that ∇p is not negligible was provided by one of the referees of this paper, who pointed out that dimples on a free surface are clearly visible far downstream in a periodic wake. An estimate of ∇p with the aid of (34) also shows that for the present model ∇p is of the same order of magnitude as the other terms in that equation. It should be mentioned that Mehta & Lavan did not compute the flow development for $Re_d = 1000$ long enough for vorticity to reach the outer boundary. With the difference approximations of (32) and (33) the values of ω and $\partial\psi/\partial\eta$ are computed on the boundary $\eta = \eta_L$:

$$\begin{aligned}\omega^{n+1}_{L,j} = \omega^{n}_{L,j}+\frac{\Delta t}{h^2_{L,j}}\bigg[&(\cos\alpha\sinh\eta_L\cos\theta_j+\sin\alpha\cosh\eta_L\sin\theta_j)\left(\frac{\omega^n_{L,j}-\omega^n_{L-1,j}}{\Delta\eta}\right)\\ &+(\sin\alpha\sinh\eta_L\cos\theta_j-\cos\alpha\cosh\eta_L\sin\theta_j)\left(\frac{\omega^n_{L,j+1}-\omega^n_{L,j-1}}{2\Delta\theta}\right)\bigg],\end{aligned} \tag{35}$$

$$\begin{aligned}\left(\frac{\partial\psi}{\partial\eta}\right)^{n+1}_{L,j} = \left(\frac{\partial\psi}{\partial\eta}\right)^{n}_{L,j} + \frac{\Delta t}{2\Delta\theta}\Bigg[&(\cos\alpha\sinh\eta_L\cos\theta_{j+1}+\sin\alpha\cosh\eta_L\sin\theta_{j+1})\frac{v^n_{\eta L,j+1}}{h_{L,j+1}} \\ &-(\cos\alpha\sinh\eta_L\cos\theta_{j-1}+\sin\alpha\cosh\eta_L\sin\theta_{j-1})\,v^n_{\eta L,j-1}/h_{L,j-1} \\ &+(\sin\alpha\sinh\eta_L\cos\theta_{j+1}-\cos\alpha\cosh\eta_L\sin\theta_{j+1})\,v^n_{\theta L,j+1}/h_{L,j+1} \\ &-(\sin\alpha\sinh\eta_L\cos\theta_{j-1}-\cos\alpha\cosh\eta_L\sin\theta_{j-1})\,v^n_{\theta L,j-1}/h_{L,j-1} \\ &+2\Delta\theta(\cos\alpha\sinh\eta_L\cos\theta_j+\sin\alpha\cosh\eta_L\sin\theta_j)\,\omega^n_{L,j}\Bigg]. \qquad (36)\end{aligned}$$

The flow is considered to be started impulsively within an infinitesimal time interval. Thus at $t = 0+$ the motion is assumed to be irrotational except at the body surface, where the no-slip condition produces a vorticity sheet. Such a singular initial condition presents problems for any numerical scheme. Series expansions have been developed to handle this situation (Görtler 1948; Wang 1967; Staniforth 1972). However, the convergence of these series is so slow, especially for thin ellipses, that their use is impractical in this study. Comparison of series expansions and numerical methods for thick ellipses shows good agreement except very close to $t = 0$ (Staniforth 1972). For thin ellipses, as will be demonstrated below, the numerical scheme produces results which agree well with experiments.

The integration process is carried out in the following way. The vorticity $\omega^{n+1}_{i,j}$ for the advanced time step $n+1$ is computed at the interior points according to (20). Next, $\omega^{n+1}_{L,j}$ and $(\partial\psi/\partial\eta)^{n+1}_{L,j}$ are determined at the downstream boundary points by means of (35) and (36). Then $\psi^{n+1}_{i,j}$ is calculated with the aid of (23). The cycle concludes with the calculation of $\omega^{n+1}_{1,j}$ from (25).

The maximum stable time step $\Delta t_{\max}$ for the DuFort–Frankel scheme, beyond which numerical instability occurs, is determined by increasing the time step until oscillations from one time step to another appear in the ω values near the tips. The magnitude of $\Delta t_{\max}$ depends on factors other than the approximation for ω_1. *It is a linear function of the Reynolds number, at least for* $Re \leqslant 200$, and decreases rapidly as either $\Delta\eta$, $\Delta\theta$ or η_1 approaches zero (Rimon 1969). There seems to be no dependence on α. If η_1 is changed from 0·05 to 0·1, $\Delta t_{\max}$ increases fourfold. For $\eta_1 = 0{\cdot}1$ and a 75×60 grid, the approximate values of $\Delta t_{\max}$ are 0·0004, 0·0007 and 0·005 for $Re = 15$, 30 and 200 respectively. Smaller time steps are necessary near $t = 0$, when the flow field changes rapidly.

The accuracy of the computations is checked by varying the size of the mesh cell and by comparing different numerical techniques.

The numerical calculation of the drag, lift and moment coefficients is achieved through the approximation of the integrals in (11)–(19). For example the second integral in the expression (12) for C_{DF} is approximated by

$$\int_0^{2\pi}\omega_1\cos\theta\,d\theta = \sum_{j=1}^{M}\Delta\theta\,\omega_{1,j}\cos\{(j-\tfrac{1}{2})\Delta\theta\}. \qquad (37)$$

Computations were carried out in double precision on an IBM 360–91 computer and in single precision on a CDC 6700 computer. The graphic display of streamlines and lines of constant vorticity was produced with a DatagraphiX

Re_d	η_1	t_{final}	Grid
15	0·1	7·2	74×60
30	0·1	20	$75 \times 60, 75 \times 64$
200	0·1	30	$75 \times 60, 75 \times 80, 75 \times 64$
200	0·2	12	75×60, 75×80
200	1·0	1·8	75×64

TABLE 1

4020 Computer Recorder. Streamlines about the elliptic cylinders are plotted for the values $\psi = 0{\cdot}1m$ where $m = \ldots -2, -1, 0, 1, 2, \ldots$. Lines of constant vorticity are constructed for $\omega = (m+\frac{1}{2})\,\Delta\omega$. For $Re = 200$, $\Delta\omega = 2$, while for the other cases $\Delta\omega = 1{\cdot}6$.

The cases computed are listed in table 1.

4. Results

In the limiting case $Re = 0$ steady-state solutions for two-dimensional flows with the boundary conditions (5) and (6) do not exist (Stokes' paradox). However, the flow characteristics for $0 < Re \ll 1$, in which case inertial forces are almost absent, can be discussed with the aid of the streamline and vorticity patterns in the central part of elongated ellipsoids for $Re = 0$. It is argued that the flow characteristics in this three-dimensional case, which represents the flow behaviour for $0 \leqslant Re \ll 1$, are similar to those of the elliptic cylinder for $0 < Re \ll 1$. Calculations were made by means of Oberbeck's integrals (Lamb 1945, p. 604) for various ellipsoids with focal-length ratios ranging from 0·1:1:1 to 0·1:1:10 where the elongated focal length is normal to the flow direction. The results show that the streamline and vorticity patterns in the plane through the centre of the body and perpendicular to the longest axis are very similar for all cases except that the flow field becomes weak for extremely stretched ellipsoids as the Stokes-paradox situation is approached. Figure 2 displays patterns for the focal-length ratio 0·1:1:5. These patterns are antisymmetric such that the flow direction is reversible. The stagnation points are situated very close to the tips, and the zero streamlines make a non-zero angle with the chord of the ellipse. As a consequence of the antisymmetry no torque is exerted on the body. The steady state is approached from the potential-flow solution in a monotonic way (Oseen 1927, p. 134). In this transient phase the stagnation points migrate from the potential-flow positions towards the tips. This pure diffusion process can be explained by the dipole-type vorticity distribution around the body (Lugt 1972), which is here distorted owing to the 45° angle of incidence. Hence, the local vorticity flux near the tips is not symmetric with respect to the chord. This situation leads to a faster decrease of the surface vorticity in the regions between each stagnation point and its nearest tip. Thus, the stagnation points are pushed towards the tips.

For $0 < Re < 1$ the steady-state drag and lift coefficients of elliptic cylinders can be obtained from the Oseen approximation of the Navier–Stokes equations.

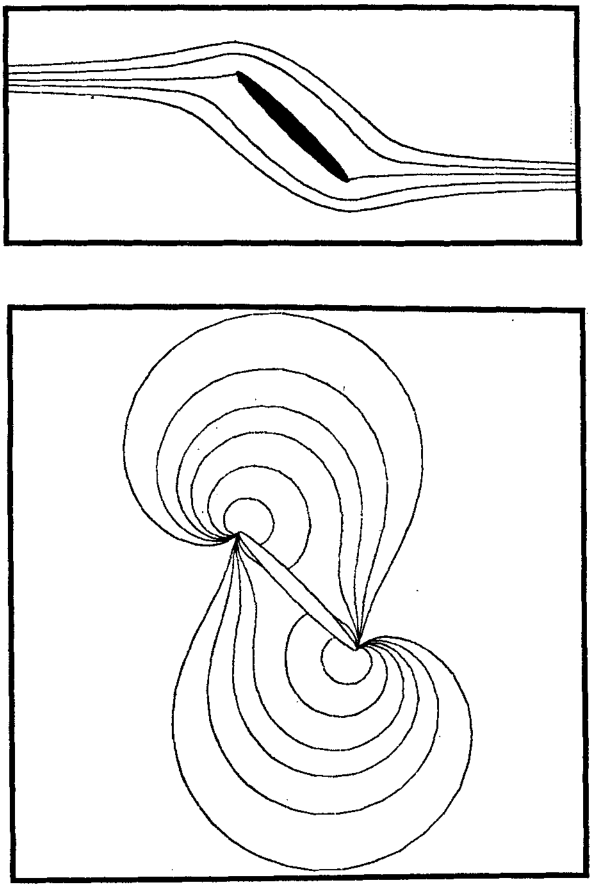

FIGURE 2. Streamlines and equi-vorticity lines around an ellipsoid with axis ratio 0·1:1:5 in the plane normal to the longest axis and passing through the centre of the ellipsoid for $Re = 0$ in the steady state.

Harrison (1924) found the solutions for $\alpha = 0$ and 90°, from which the values for an elliptic cylinder at 45° incidence can be computed by superposition.

For non-zero Reynolds numbers inertial effects manifest themselves in a distortion of the vorticity generation and spreading. The antisymmetry is lost. In front of the body vorticity spreading is suppressed, in the rear spreading is supported. The suppression of the vorticity spreading in front counteracts the movement of the front stagnation point from its potential-flow position towards the tip. The steady-state location of the stagnation point is between the tip and its potential-flow location. The movement of the rear stagnation point to the trailing tip is aided by the inertial effects. On the surface the pressure is directly related to the vorticity flux. Immediately after the impulsive start, that is at $t = 0+$, the pressure has a minimum at the rear stagnation point, which is not yet at the tip. It is emphasized that the surface pressure at $t = 0+$ is not determined by the potential flow but by the vorticity sheet adjacent to the surface. In this sheet $(\partial\omega/\partial\eta)_1$ changes sign at the front and rear stagnation points and thus

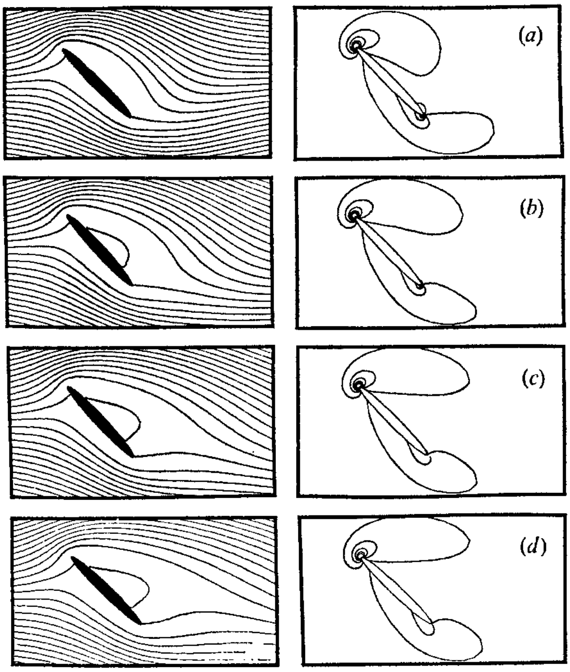

FIGURE 3. Sequence of streamlines and equi-vorticity lines for $Re = 15$, $\eta_1 = 0\cdot 1$ at various times after the abrupt start. Potential flow at $t = 0$.

	(a)	(b)	(c)	(d)
t	1·79	3·79	5·39	6·39
C_D	−5·15	−4·59	−4·39	−4·27
C_L	−2·89	−2·86	−2·73	−2·62
C_M	−1·74	−1·52	−1·41	−1·37

makes p_1 a maximum and a minimum, respectively, according to (8). After a short time, from a certain Reynolds number on, a second local pressure minimum appears at the trailing tip. The numerical results show that when $\eta_1 = 0\cdot 1$ this phenomenon occurs at least for $Re \geqslant 15$. The second minimum grows in relation to the minimum at the stagnation point and by the time the stagnation point reaches the tip again only one minimum is present. The increase in vorticity flux to the rear of the body leads to the formation of regions of recirculatory flow, depending on the curvature of the ellipse and the value of the Reynolds number. For the circular cylinder ($\eta_1 = \infty$), in the steady state a recirculatory region occurs first at approximately $Re = 3$. The flow about an infinitely thin body with $\eta_1 = 0$ may have a recirculatory region for any $Re > 0$. In the transient phase recirculatory regions first appear near the tips for thin ellipses and near the centre for thick ellipses (Görtler 1948; Wang 1967; Staniforth 1972). In figure 3 streamlines and lines of equal vorticity are shown for $Re = 15$ and $\eta_1 = 0\cdot 1$ during the period $0 < t < 7$. Although at $t_{\text{final}} = 7$ the 'almost steady state' has not yet been reached, the tendency towards a steady-state solution is clearly demonstrated. The change in the flow field when time advances from $t = 5\cdot 39$ to $t = 7$ is so small

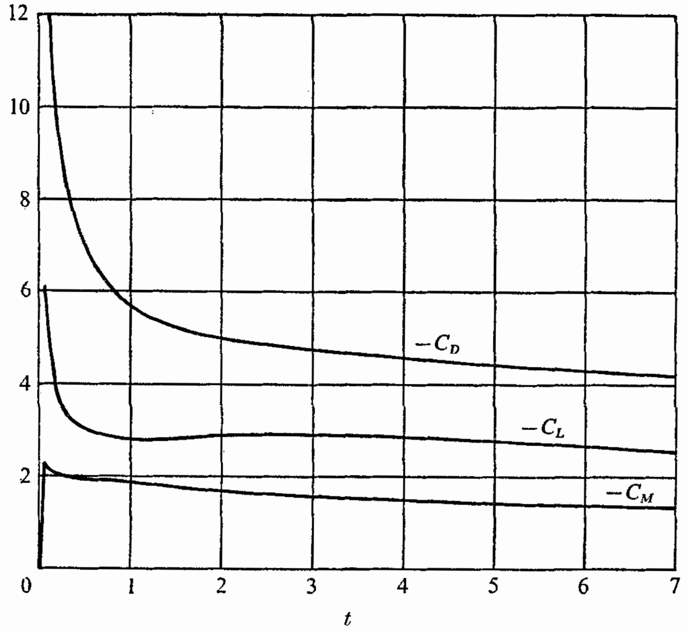

FIGURE 4. Drag, lift and moment coefficients *vs.* time for $Re = 15$, $\eta_1 = 0{\cdot}1$ after the abrupt start.

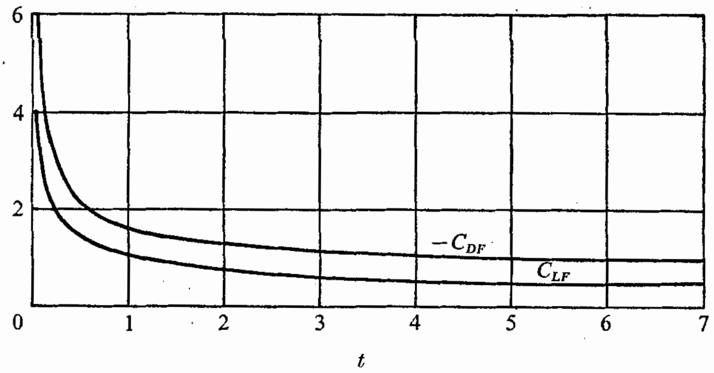

FIGURE 5. Coefficients for frictional drag and lift *vs.* time for $Re = 15$, $\eta_1 = 0{\cdot}1$ after the abrupt start.

that plots of flow patterns for these times are indistinguishable. The monotonic approach towards a steady state is also demonstrated in the curves for C_D, C_L, C_M, C_{DF} and C_{LF} in figures 4 and 5. The abrupt start of the body during the infinitesimal time interval from $t = 0-$ to $t = 0+$ requires infinite values for C_D as well as for C_L, whereas C_M is zero. The unbounded value for C_L is not obvious but can be explained with the aid of (15) and (16). Since diffusion dominates convection at that moment the vorticity and hence C_D and C_L can be computed near $t = 0$ with a Taylor series expansion in $t^{-\frac{1}{2}k}$ by means of a boundary-layer transformation for the vorticity and the η co-ordinate. This was demonstrated

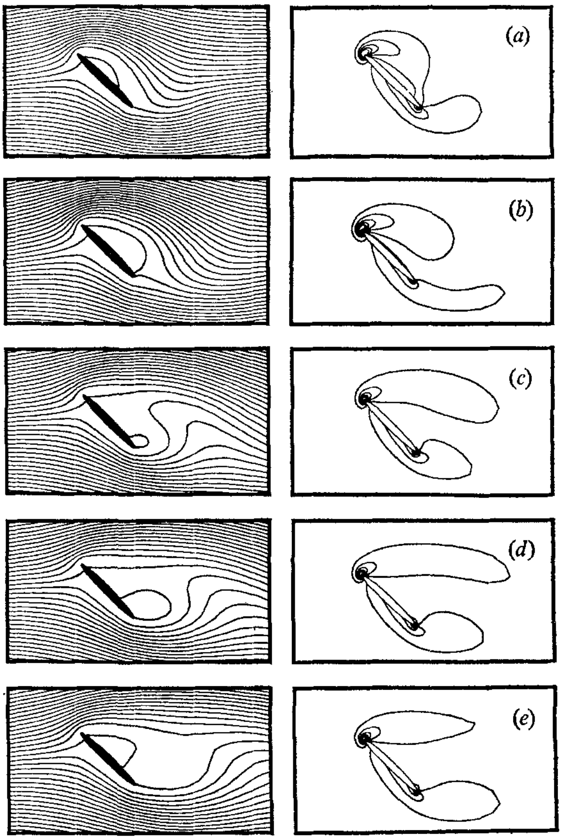

FIGURES 6(*a*)–(*e*). For legend see next page.

by Staniforth (1972), who found that C_D and C_L are proportional to $t^{-\frac{1}{2}}$ near $t = 0$. Staniforth also pointed out the erroneous theoretical prediction by Wang (1967) of zero lift immediately after the impulsive start. Mehta & Lavan (1972) also found an unbounded value for C_L. The hump in C_L arises from the fact that C_{LP} and C_{LF} have opposite signs. At both early and late times the change in C_L is dominated by the change in C_{LP}. However, during an intermediate time interval C_{LF} is changing so rapidly relative to C_{LP} that the change in C_L has the same sign as the change in C_{LF}. The hump in the C_M curve can be explained by the symmetry associated with the starting conditions. While the values of the force coefficients are infinite at $t = 0$ owing to the impulsive start, the initial symmetry results in zero torque. As this symmetry is lost in the early development, C_M increases rapidly since the vorticity and vorticity gradient are large on the body surface. Later, as the initial large vorticity values decrease, C_M decreases toward its steady-state value.

When the Reynolds number is increased to 30 the steady state is approached in an oscillatory manner (figure 6). During the transient phase regions of recirculatory flow are formed alternately behind the leading and trailing tips. However, vortex shedding does not occur, in the sense that the alternate formation of

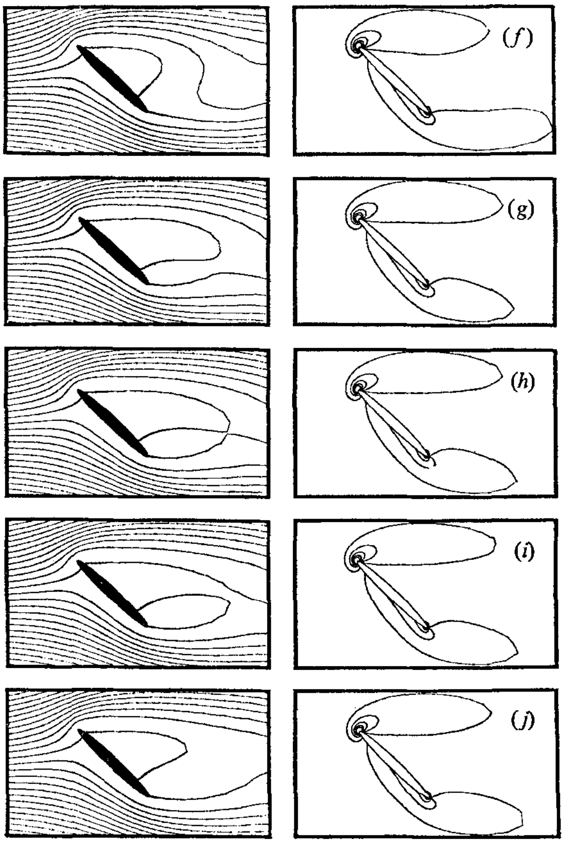

FIGURE 6. Some patterns of streamlines and equi-vorticity lines for $Re = 30$, $\eta_1 = 0{\cdot}1$ at various times after the abrupt start. Potential flow at $t = 0$.

	(*a*)	(*b*)	(*c*)	(*d*)	(*e*)	(*f*)	(*g*)	(*h*)	(*i*)	(*j*)
t	1·59	3·27	6·51	8·13	9·75	12·0	16·0	17·0	18·0	20·2
C_D	—	—	—	—	—	—	−2·92	−2·91	−2·89	−2·86
C_L	—	—	—	—	—	—	−1·93	−1·91	−1·90	−1·87
C_M	—	—	—	—	—	—	−1·01	−1·01	−1·01	−1·01

recirculatory flow regions is not accompanied by the formation of vorticity extrema. Figure 7 displays time histories of C_{DF} and C_{LF}, which also exhibit the oscillatory approach to a steady state.

Dumitrescu & Cazacu (1970) published numerical solutions for steady flows past a flat plate with $\eta_1 = 0$ and $\alpha = 45°$ within a channel for $Re = 15$ and 25. The streamline patterns are similar to those of figure 3 (*d*) and figure 6 (*j*) except for the separation at the leading edge which is present when $\eta_1 = 0$. Only one closed-streamline region exists behind the body in contrast to the case $\alpha = 90°$, where two steady wake vortices occur. Somewhere in the range $45° < \alpha < 90°$ the recirculatory region behind the rear tip opens up as α decreases.

At about $Re = 45$ the steady state becomes unstable, and the flow changes to a stable mode in the form of the Kármán vortex street. Although the critical Reynolds number of 45 is verified for circular cylinders only, indications are that

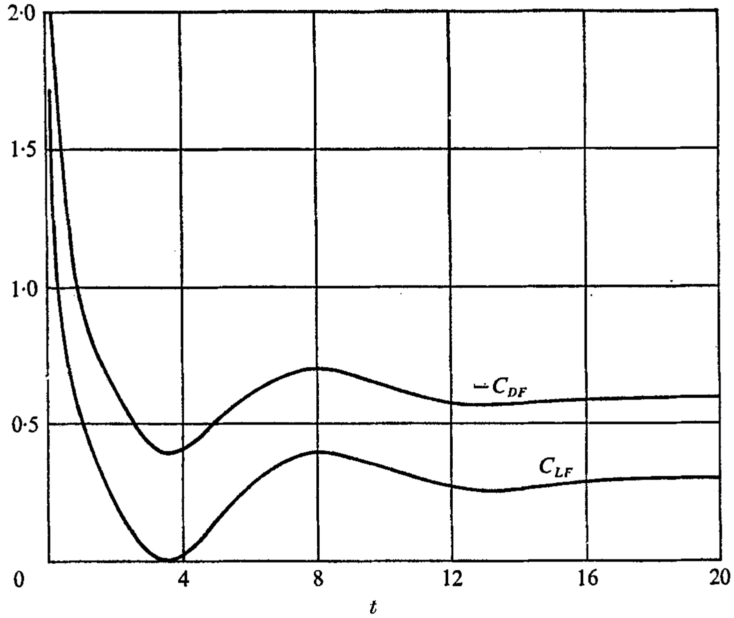

Figure 7. Coefficients for frictional drag and lift *vs.* time for $Re = 30$, $\eta_1 = 0{\cdot}1$ after the abrupt start.

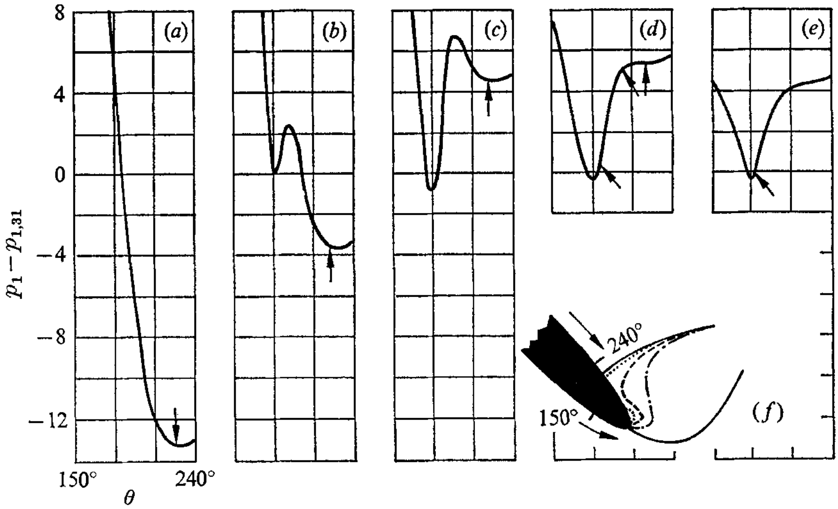

Figure 8. The establishment of the Kutta condition in viscous fluids for $Re = 200$. Arrows indicate stagnation and separation points. $p_{1,31}$ is p_1 at $\theta = 183°$. (*a*) $t = 0{\cdot}004$. (*b*) $t = 0{\cdot}006$. (*c*) $t = 0{\cdot}012$. (*d*) $t = 0{\cdot}036$. (*e*) $0{\cdot}060$. In (*f*), —, $t = 0, 0{\cdot}04$; ····, $t = 0{\cdot}036$; ----, $t = 0{\cdot}06$; —·—, $t = 0{\cdot}1$.

this number might be valid for any blunt body or flat plate at an angle of attack beyond stall. To study the transient phase from $t = 0$ to a Kármán vortex street the Reynolds number 200 is selected.

During the initial phase $0 < t < 0{\cdot}5$ the flow development is basically similar to that which occurs for $Re = 15$ and 30. However, the inertial effects are much

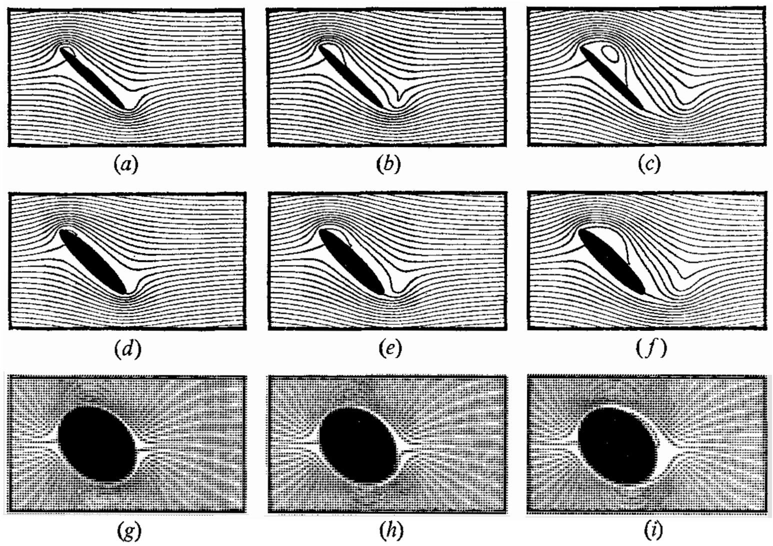

FIGURE 9. Streamlines in the initial phase of wake development for $Re_a = 200$ and various η_1.

	(a)	(b)	(c)	(d)	(e)	(f)	(g)	(h)	(i)
η_1	0·1	0·1	0·1	0·2	0·2	0·2	1·0	1·0	1·0
t	0·300	0·612	1·48	0·315	0·675	1·46	0·300	0·600	1·50
C_D	−4·30	−3·68	−3·56	−3·75	−3·13	−3·09	−15·6	−3·91	−2·16
C_L	−3·59	−3·68	−4·00	−2·42	−3·09	−3·70	−0·846	−0·284	−0·725
C_M	−2·10	−1·90	−1·83	−2·20	−1·94	−1·75	−0·989	−1·26	−1·08

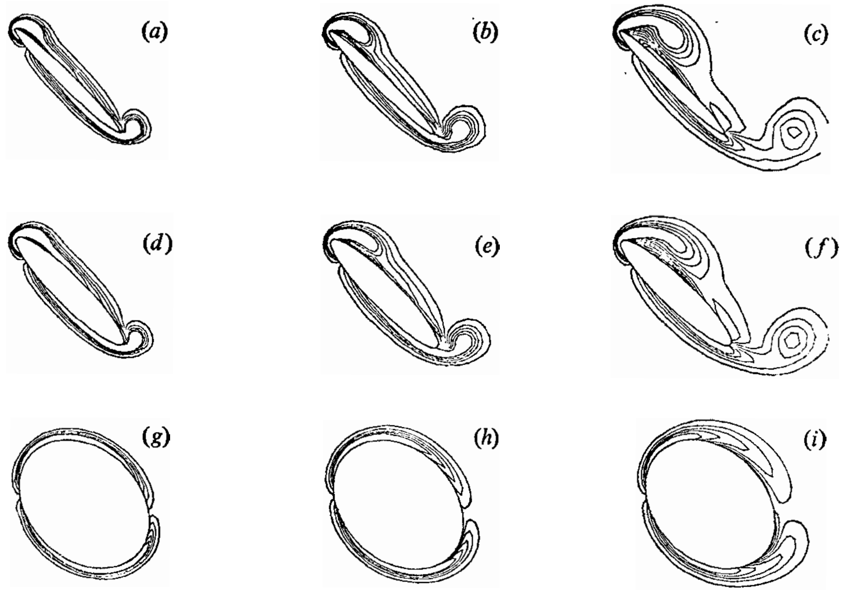

FIGURE 10. Equi-vorticity lines in the initial phase of wake development for $R_a = 200$ and various η_1. Conditions for (a)–(i) as in figure 9.

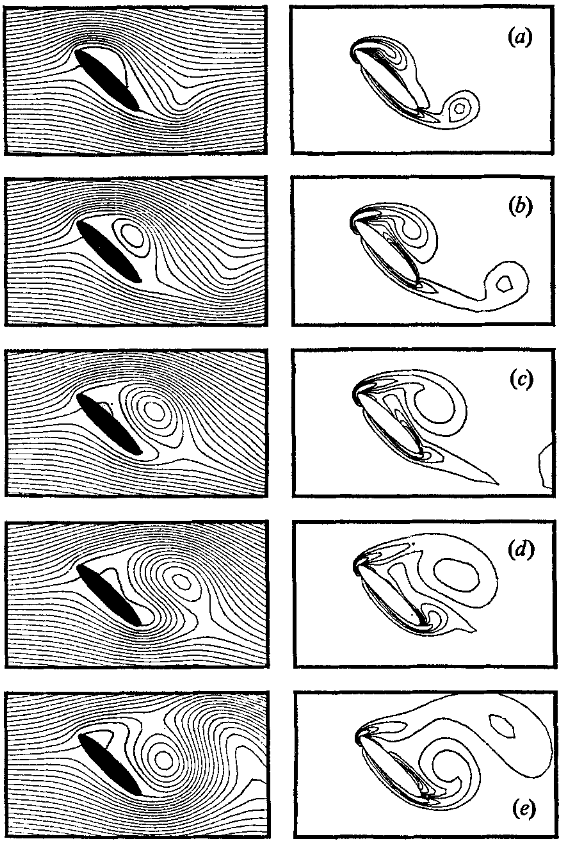

FIGURE 11. Patterns of streamlines and equi-vorticity lines for $Re_d = 200$, $\eta_1 = 0{\cdot}2$ after the abrupt start. Potential flow at $t = 0$.

	(a)	(b)	(c)	(d)	(e)
t	1·68	3·17	4·79	6·41	8·84
C_D	−3·13	−3·47	−3·16	−2·70	−2·68
C_L	−3·81	−4·06	−2·88	−1·15	−1·17
C_M	−1·72	−1·24	−0·734	−0·582	−0·560

more pronounced when $Re = 200$. The local pressure minimum which forms at the tip for $Re = 15$ and 30 becomes so strong at $Re = 200$ that the flow separates from the surface just behind the tip (figure 8). At first the flow reattaches to the surface and forms a small recirculatory region as displayed in figure 8(*f*) for $\eta_1 = 0{\cdot}1$ at $t = 0{\cdot}036$. This region grows in extent as, simultaneously, the zero streamline moves towards the tip. By $t = 0{\cdot}06$ there is again only one rear stagnation point. It moves towards the tip, and by $t = 0{\cdot}4$ the zero streamline is aligned parallel to the chord of the ellipse. This situation is called the Kutta condition for viscous media (Thwaites 1960). This transient development represents the formation and shedding of a starting vortex, a phenomenon which is well known from flow photographs at high Reynolds numbers. For $\eta_1 = 0{\cdot}1$ the computed results show a vorticity extremum, which first appears sometime between $t = 0{\cdot}1$ and $t = 0{\cdot}2$,

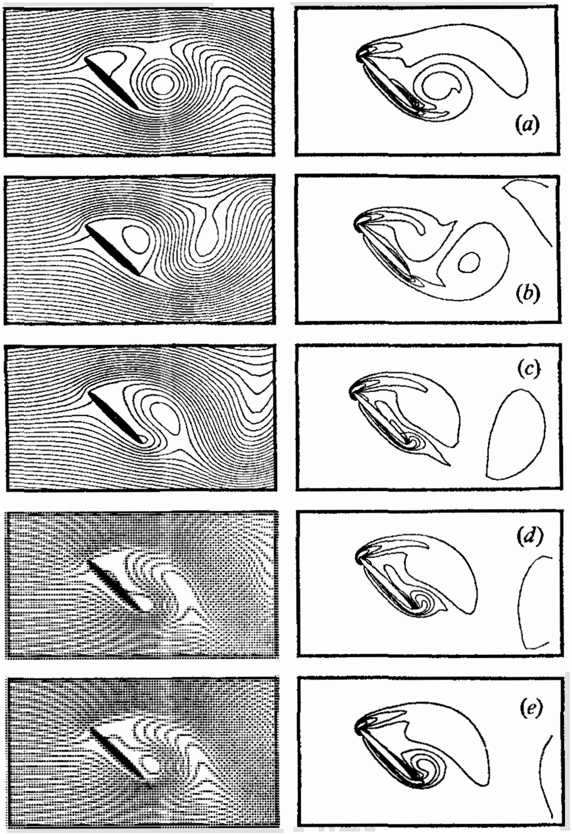

FIGURE 12. Sequence of streamlines and equi-vorticity lines for the third cycle for $Re = 200$, $\eta_1 = 0\cdot 1$ after the abrupt start.

	(*a*)	(*b*)	(*c*)	(*d*)	(*e*)
t	17·8	20·3	22·4	23·2	24·1
C_D	−2·46	−3·01	−3·13	−3·10	−2·97
C_L	−1·62	−3·09	−2·56	−2·12	−1·82
C_M	−0·618	−0·931	−0·657	−0·501	−0·381

to the rear of the trailing tip. This starting vortex is visible as a region of highly curved streamlines moving relative to the body (figures 9 and 10). After separation of the starting vortex, another region of recirculatory flow forms behind the front tip. All these phenomena are modified or do not occur at all in flows past fat bodies.

After the initial phase a Kármán vortex street develops. A sequence of streamlines and lines of equal vorticity for the first cycle is shown in figure 11 for $\eta_1 = 0\cdot 2$. Here a cycle is defined to be the event which commences with the shedding of a vortex from the leading tip and ends with the shedding of the next vortex from this same point. The flow patterns for $\eta_1 = 0\cdot 1$ have been published already in Lugt & Haussling (1971). These solutions are quite similar.

The third cycle for $\eta_1 = 0\cdot 1$ is displayed in figure 12. The development and the detachment of the vortices are similar to those of the first cycle. By the end

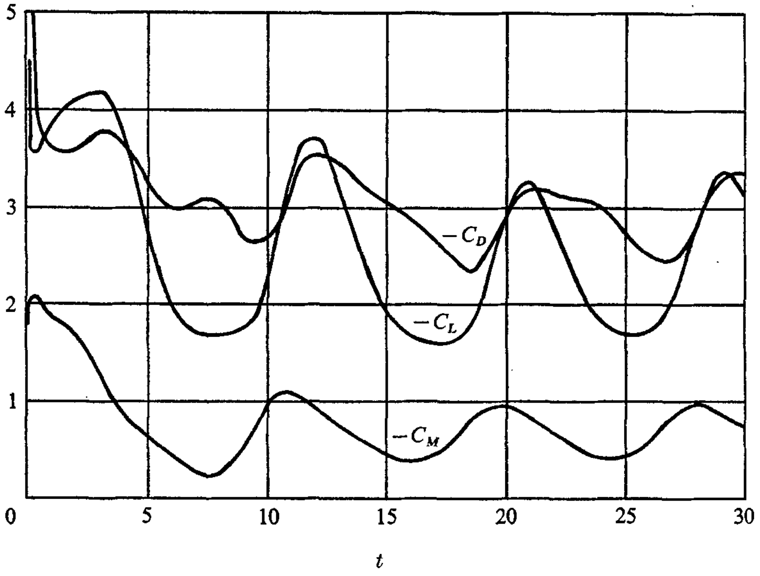

FIGURE 13. Drag, lift and moment coefficients *vs.* time for $Re = 200$, $\eta_1 = 0{\cdot}1$ after the abrupt start.

of the third cycle at $t \approx 30$ the initial vortex has crossed the outer boundary of the grid.

In figure 13 the drag, lift and moment coefficients are plotted against time t. The abrupt start of the body requires infinite values for C_D and C_L, whereas C_M begins from zero. The Strouhal number, which is defined by

$$St = dn/U, \tag{38}$$

is about 0·23 for the second cycle and 0·25 for the third. In (38) n is the frequency of the vortex shedding measured in cycles per unit time. If one relates the Strouhal number to the projected plate width $d \sin \alpha$, the values for the second and third cycles are 0·163 and 0·177, respectively.

For $\eta_1 = 0{\cdot}2$ computations have been made with $\Delta\theta = \frac{1}{30}\pi$ as well as with $\Delta\theta = \frac{1}{40}\pi$. The differences in the C_D, C_L and C_M values between the two cases are so small that they cannot be observed on a graphic display.

In figure 14 the coefficients C_{DF} and C_{LF} are plotted against time for $Re = 200$ and $\eta_1 = 0{\cdot}1$. The surface pressure p_1 is displayed in figure 15 for the third cycle for $Re = 200$ and $\eta_1 = 0{\cdot}1$. During this time the pressure at the stagnation point varies between the values 0·533 and 0·558. The value in the inviscid limit is 0·5.

The information contained in figures 11–15 permits the following physical interpretation of the relation between vortex shedding and the force and moment coefficients.

Since $C_{DP}, C_{LP} \gg C_{DF}, C_{LF}$ the main characteristics of the curves for C_D and C_L should be explainable by the behaviour of C_{DP} and C_{LP}. Equations (11), (13) and (15) show that for $\alpha = 45°$ and for $\eta \ll 1$ the curves of C_{DP} and C_{LP} should not deviate much from one another. In particular, since one vortex is shed from each

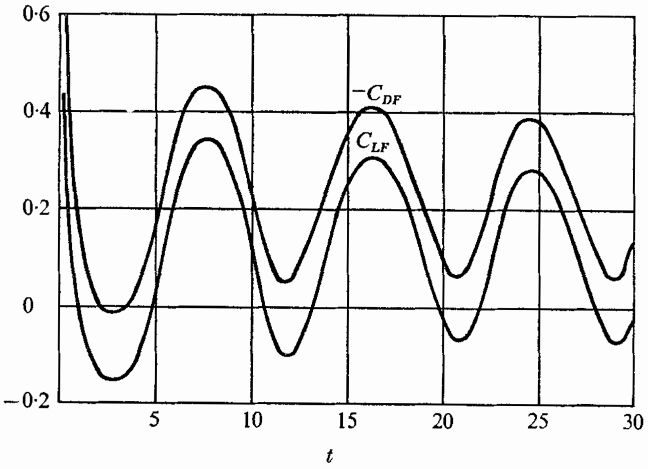

FIGURE 14. Coefficients for frictional drag and lift *vs.* time for $Re = 200$, $\eta_1 = 0{\cdot}1$ after the abrupt start.

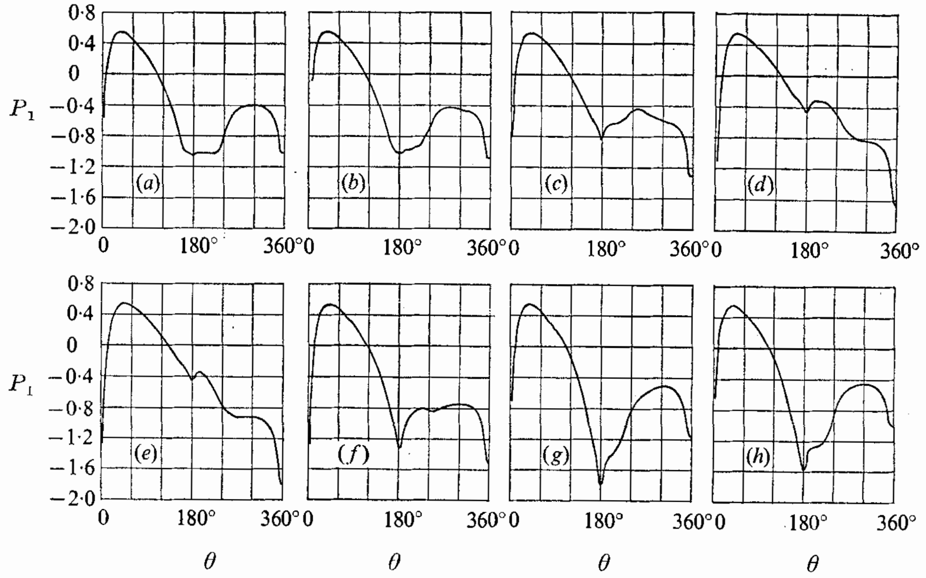

FIGURE 15. Surface pressure versus θ for the third cycle for $Re = 200$, $\eta_1 = 0{\cdot}1$.

	(*a*)	(*b*)	(*c*)	(*d*)	(*e*)	(*f*)	(*g*)	(*h*)
t	16·6	17·4	18·5	19·8	20·7	22·1	23·6	24·5
C_D	−2·77	−2·57	−2·30	−2·75	−3·14	−3·14	−3·06	−2·89
C_L	−1·60	−1·57	−1·73	−2·71	−3·25	−2·76	−1·97	−1·75
C_M	−0·396	−0·156	−0·790	−0·972	−0·871	−0·695	−0·434	−0·378

tip during one cycle the curves of C_{DP} and C_{LP} should exhibit two periods per cycle. However, a brief look at figure 13 reveals that the periods for all curves coincide with the duration of a cycle, and that the difference between C_D and C_L is quite large. The explanation of this seeming discrepancy may be started with a discussion of the local maxima of $-C_D$ and $-C_L$ (which coincide with those of $-C_{DP}$ and $-C_{LP}$) at $t = 3{\cdot}2$, $12{\cdot}0$, $21{\cdot}0$ and $29{\cdot}0$. A comparison of figure 13 with figures 11, 12 and 15 reveals that these local maxima occur just when the recirculatory region developed behind the front tip separates from the body. This event is defined by the appearance of a vorticity extremum and marks the end of the roll-up of vorticity and the beginning of vortex shedding. In figure 11(*b*) and figure 12(*b*), the extrema are indicated by the tongue-shaped equi-vorticity lines. The existence of these extrema is verified by the complete computer output. The recirculatory region which at the moment of separation reaches its largest extent is associated with a maximum p_1-difference between the areas around $\theta = 90°$ and $\theta = 270°$. They contribute most to C_{DP} and C_{LP} according to (11), (13) and (15). At $t = 7{\cdot}5$ in figure 13 a local maximum in C_D occurs which can be related to the moment of separation of the recirculatory region developed behind the rear tip. Although this maximum is small compared with the previously discussed maxima, the anticipated period of a half-cycle is visible in the C_D curve for the first cycle. The small size of this maximum is explained by the strong influence of the already shed front-tip vortex on the formation and separation of the recirculatory region behind the rear tip. If one examines C_{LP} by subtracting C_{LF} from C_L such a small maximum also exists for C_{LP} at $t = 7{\cdot}5$. From the second cycle on, the small local maximum does not appear. It has degenerated to a small hump in C_D as well as in C_{DP}. This is due to the influence of the previously shed vortices. It may be pointed out that in Mehta & Lavan's (1972) results for $Re_d = 1000$ and $\alpha = 15°$ the above-mentioned small maxima in the C_D and C_L curves during the first cycle are more pronounced than in the present result owing to the smaller influence of viscosity at $Re_d = 1000$.

The coefficient of C_M is always negative. This means that the torque tends to turn the broadside of the body perpendicular to the main stream. The maxima and minima of C_M are located a little before those of C_L. These occur when the surface pressure in the rear has its largest and smallest asymmetric distribution with respect to the centre of the body.

On the basis of experiments (Timme 1957) the decay of vortices in the Kármán vortex street can be described by the Hamel–Oseen solution for each vortex:

$$v'_\phi = \frac{\text{constant}}{r}\left(1-\exp\{-r^2/4\nu(t'-t'_0)\}\right), \quad v'_r \equiv 0, \tag{39}$$

where the polar co-ordinates (r, ϕ) with the corresponding velocity components (v'_r, v'_ϕ) are used. Equation (39) represents the decay of a potential vortex from the time $t' = t'_0$. This expression represents the lowest mode of plane disturbances (Lugt 1968). The vorticity at the vortex centre (where the extremum of vorticity is located) is dissipated according to

$$\omega'_{r=0} = \text{constant}/2\nu(t'-t'_0). \tag{40}$$

For the next higher mode of the spectrum of disturbances the vorticity $\omega'_{r=0}$ would decay as $(t'-t'_0)^{-2}$ (Lugt 1968). The numerical data can be checked against the analytic prediction. In figure 16 the decay of the central vorticity of the initial vortex for $Re = 200$ and $\eta_1 = 0{\cdot}1$ is displayed with logarithmic scales. The best fit to a linear relation between the logarithms of the central vorticity and time is

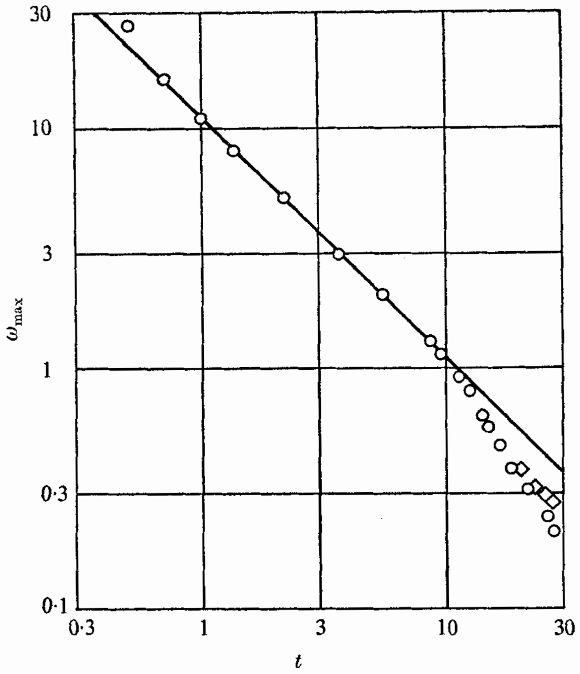

FIGURE 16. Decay of central vorticity of the initial vortex for $Re = 200$, $\eta_1 = 0{\cdot}1$. ○, 75 × 60 grid; ◇, 75 × 80 grid in third cycle.

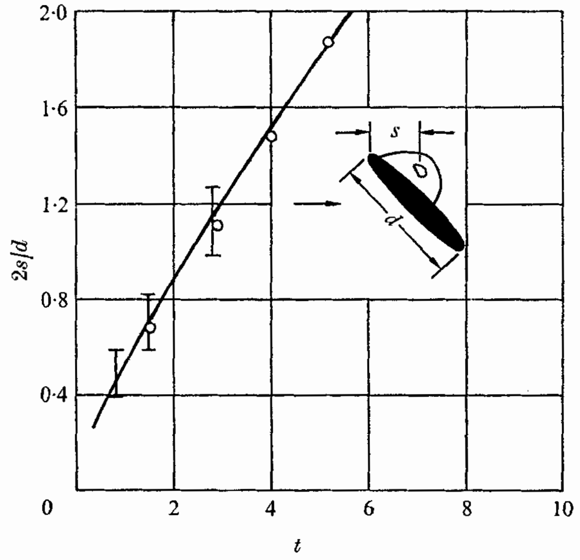

FIGURE 17. Comparison of numerical results for $Re = 200$, $\eta_1 = 0{\cdot}1$ with experimental data. ○, experiments (Honji); ⌶, uncertainty in $2s/d$ due to grid spacing.

obtained when $t_0 = -0{\cdot}3$ and the slope is -1. Vortices which are generated after the initial vortex behave similarly. Near the outer boundary of the grid, where the mesh size increases rapidly, the numerical values deviate from the analytic curve. This deviation depends on the mesh size (figure 16). Possibly, the numerical solution is not accurate enough to describe the vortex decay in that part of the grid.

For $Re_d = 1000$ Mehta & Lavan's (1972) data for a symmetric airfoil with 9 % thickness are available. A comparison of their results with the present ones must take into consideration the difference in α. For $\alpha = 15°$ the potential-flow stagnation points are closer to the tips than for $\alpha = 45°$. The evolution of the Kutta condition in the initial phase is, thus, confined to a smaller surface area. Nevertheless, this condition is established at about the same time ($t \approx 0{\cdot}4$) for $Re_d = 1000$ and $\alpha = 15°$ as for $Re_d = 200$ and $\alpha = 45°$. A detailed description of the pertinent literature on the generation of lift for high Re_d (of Prandtl & Tietjens, Goldstein and Batchelor) can also be found in Mehta & Lavan's paper. The process of vortex shedding is similar for $Re_d = 1000$ with $\alpha = 15°$ and $Re_d = 200$ with $\alpha = 45°$ although the spacing of the shed vortices in the direction normal to the flow is smaller for $\alpha = 15°$ than for $\alpha = 45°$.

Honji (1972) compared flow photographs with streamline patterns from the authors' numerical data. The result is shown in figure 17, where the position of the first vortex behind the front tip is plotted against time.

The authors would like to thank Mr S. Ohring for his assistance in programming the various computer codes. They also owe thanks to J. K. Reingruber and R. T. Van Eseltine for devising a code to compute Oberbeck's integral and to one of the reviewers who furnished constructive criticism and valuable comments.

REFERENCES

Berger, E. & Wille, R. 1972 Periodic flow phenomena. *Ann. Rev. Fluid Mech.* **4**, 313.

Buzbee, B. L., Golub, G. H. & Nielson, C. W. 1970 On direct methods for solving Poisson's equations. *SIAM J. Numer. Anal.* **7**, 627.

Dawson, C. & Marcus, M. 1970 DMC – a computer code to simulate viscous flow about arbitrarily shaped bodies. *Proc.* 1970 *Heat Transfer & Fluid Mech. Inst.*, p. 323. Stanford University Press.

Dumitrescu, D. & Cazacu, M. D. 1970 Theoretische und experimentelle Betrachtungen über die Strömung zäher Flüssigkeiten um eine Platte bei kleinen und mittleren Reynoldszahlen. *Z. angew. Math. Mech.* **50**, 257.

Görtler, H. 1948 Grenzschichtentstehung an Zylindern bei Anfahrt aus der Ruhe. *Arch. Math.* **1**, 138.

Harrison, W. J. 1924 On the motion of spheres, circular and elliptic cylinders through viscous liquid. *Trans. Camb. Phil. Soc.* **23**.

Hockney, R. W. 1970 The potential calculation and some applications. *Methods in Comp. Phys.* **9**, 135.

Honji, H. 1972 Starting flows past spheres and elliptic cylinders. *Rep. Res. Inst. Appl. Mech., Kyushu University*, **19**, 271.

Krzywoblocki, M. Z. v. 1966 Vortex streets in fluids. In *Applied Mechanics Surveys* (ed. M. N. Abramson *et al.*), p. 885. Washington: Spartan Books.

Lamb, H. 1945 *Hydrodynamics*, 6th edn. Dover.

Lugt, H. J. 1968 The spectrum of the final decay of localized disturbances in a viscous fluid. *Naval Ship R. & D. Center Rep.* no. 2785.

Lugt, H. J. 1972 Entstehung und Ausbreitung von Wirbeln unter der 'Perfect-Slip' Bedingung. *Dtsch. Luft- & Raumfahrt, Forschungsbericht,* no. 72–27, p. 259.

Lugt, H. J. & Haussling, H. J. 1971 Laminar flows past a flat plate at various angles of attack. *Lecture Notes in Physics,* vol. 8, p. 78. Springer.

Lugt, H. J. & Haussling, H. J. 1972 Transient Ekman and Stewartson layers in a rotating tank with a spinning cover. *Recent Research on Unsteady Boundary Layers,* p. 1366. Québec: Laval University Press.

Lugt, H. J. & Ohring, S. 1971 Laminar flows past an infinitely thin disk. *Naval Ship R. & D. Center Rep.* no. 3654.

Lugt, H. J. & Ohring, S. 1973 Efficiency of numerical methods in solving the time-dependent two-dimensional Navier–Stokes equations. *Proc. Int. Conf. on Numerical Methods in Fluid Dyn., Southampton.*

Lugt, H. J. & Rimon, Y. 1970 Finite-difference approximations of the vorticity of laminar flows at solid surfaces. *Naval Ship R. & D. Center Rep.* no. 3306.

Mehta, U. B. & Lavan, Z. 1972 Starting vortex, separation bubbles and stall – a numerical study of laminar unsteady flow around an airfoil. *AFOSR Tech. Rep.* AFOSR-TR-73-0640. (See also *Themis Rep.* R 72-11, I.I.T.)

Morkovin, M. V. 1964 Flow around circular cylinder – a kaleidoscope of challenging fluid phenomena. *Symp. on Fully Separated Flows,* p. 102. A.S.M.E.

Oseen, C. W. 1927 *Hydrodynamik.* Leipzig: Akademische Verlagsgesellschaft.

Rimon, Y. 1969 Numerical solution of the incompressible time-dependent viscous flow past a thin oblate spheroid. *Phys. Fluids Suppl.* **12**, II-65.

Roache, P. J. 1972 *Computational Fluid Dynamics.* Albuquerque: Hermosa Publishers.

Staniforth, A. N. 1972 Ph.D. dissertation, Dept. Appl. Math., University of Western Ontario.

Timme, A. 1957 Über die Geschwindigkeitsverteilung in Wirbeln. *Ing. Arch.* **25**, 205.

Thwaites, B. (ed.) 1960 *Incompressible Aerodynamics,* p. 179. Clarendon Press.

Wang, C. 1967 Separation and stall of an impulsively started elliptic cylinder. *J. Appl. Mech.* **34**, 823.